Article

Controlling Charge Transport in 2D Conductive MOFs—The Role of Nitrogen-Rich Ligands and Chemical Functionality

Petru Apostol,* Sai Manoj Gali, Alice Su, Da Tie, Yan Zhang, Shubhadeep Pal, Xiaodong Lin, Vasudeva Rao Bakuru, Darsi Rambabu, David Beljonne, Mircea Dincă, and Alexandru Vlad*

Read Online

ACCESS | Metrics & More | Article Recommendations | Supporting Information

ABSTRACT: Two-dimensional electrically conducting metal−organic frameworks (2D-e-MOFs) have emerged as a class of highly promising functional materials for a wide range of applications. However, despite the significant recent advances in 2D-e-MOFs, developing systems that can be postsynthetically chemically functionalized, while also allowing fine-tuning of the transport properties, remains challenging. Herein, we report two isostructural 2D-e-MOFs: $Ni_3(HITAT)_2$ and $Ni_3(HITBim)_2$ based on two new 3-fold symmetric ligands: 2,3,7,8,12,13-hexaaminotriazatruxene (HATAT) and 2,3,8,9,14,15-hexaaminotribenzimidazole (HATBim), respectively, with reactive sites for postfunctionalization. $Ni_3(HITAT)_2$ and $Ni_3(HITBim)_2$ exhibit temperature-activated charge transport, with bulk conductivity values of 44 and 0.5 mS cm^{-1}, respectively. Density functional theory analysis attributes the difference to disparities in the electron density distribution within the parent ligands: nitrogen-rich HATBim exhibits localized electron density and a notably lower lowest unoccupied molecular orbital (LUMO) energy relative to HATAT. Precise amounts of methanesulfonyl groups are covalently bonded to the N−H indole moiety within the $Ni_3(HITAT)_2$ framework, modulating the electrical conductivity by a factor of ~20. These results provide a blueprint for the design of porous functional materials with tunable chemical functionality and electrical response.
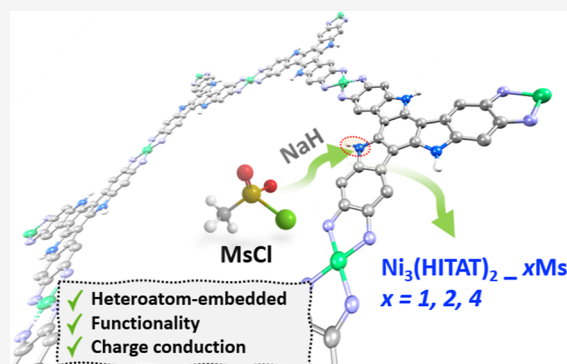
INTRODUCTION

Over the last few decades, major interest has been devoted to new classes of electrically conducting materials, either of organic, inorganic, or mixed composition.[1] In the quest to develop new functional and cost-effective materials with high structural tunability for applications in electronics, energy storage,[2,3] catalysis,[4] and sensing materials,[5] metal−organic frameworks (MOFs) have gained considerable traction. For many years, MOFs have been considered as electrical insulators, preventing their integration with an electrical stimulus. Recent developments nevertheless have shown that electrical conductivity in MOFs is possible and is strongly correlated to chemical composition, the nature of the metal ions, the organic linkers, and their binding modes.[1] The most common strategies for tuning the electronic conductivity rely on the use of redox-active ligands to promote the generation of charge carriers[6] and metal centers to foster charge transfer from the ligand to the metal through enhanced orbital overlap. Additionally, $\pi-\pi$ stacking interactions between layers [characteristic of two-dimensional (2D)-MOFs][1] as well as electrochemical doping (e.g., oxidation or reduction)[7] can be used to modulate the electronic conductivity of MOFs.

Conjugated 2D-e-MOFs, as a subclass of conducting MOFs, are composed of square-planar late transition metals (i.e., Ni, Cu, Co, or Pt) and extended planar aromatic ligands. The combination of planar linkers with four-coordinate square-planar metal ions results in 2D layered structures with extended conjugation, which permits extended delocalization of charge carriers. Additional $\pi-\pi$ stacking interactions between layers lead to remarkable electronic conductivity values, approaching 10 S cm^{-1} (bulk) and exceeding 150 S cm^{-1} (single crystals).[1,6,8] These remarkable attributes render the class of 2D-e-MOFs highly suitable for implementation in research domains where their inherent electrical insulation had been previously considered as a limitation, such as electrocatalysis, energy storage, and sensing.[9−12] However, the chemistry of the 2D-e-MOFs has been long considered locked,[13−15] given the inflexibility of metal ion geometry and the chemically inert nature of the ligands, which are typically made of benzene,[16] triphenylene,[17,18] or phthalocyanine[19,20] cores.

A

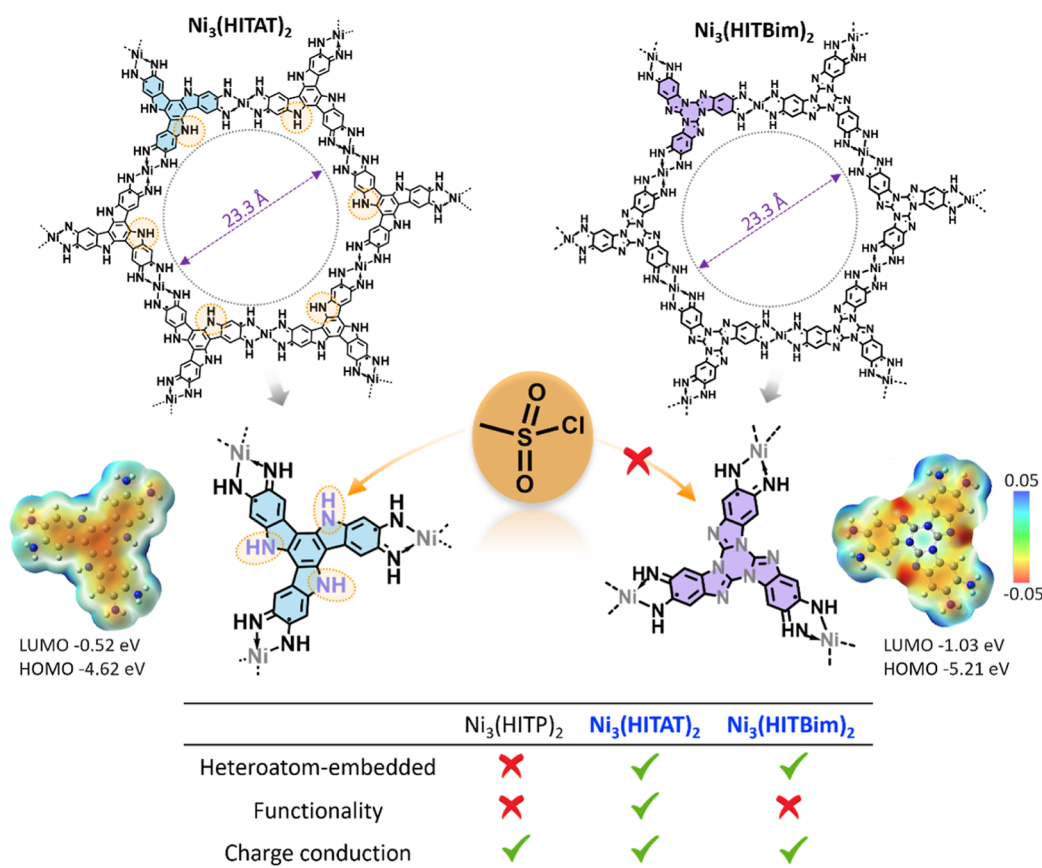**Figure 1.** Molecular design of $Ni_3(HITAT)_2$ and $Ni_3(HITBim)_2$ MOFs (top). Molecular electrostatic potential maps of the corresponding ligands HATAT and HATBim and the computed HOMO and LUMO levels highlight the electron-deficient character of the HATBim as compared to HATAT. (bottom table) Comparative analysis of key properties between archetypal $Ni_3(HITP)_2$ and the $Ni_3(HITAT)_2$ as well as $Ni_3(HITBim)_2$ MOFs presented in this work.

To the best of our knowledge, the first example of chemically functional 2D-e-MOFs has been reported only recently by J. Park et al.[21] The authors designed an MOF based on a supramolecular linker, e.g., 2,3,8,9,14,15-hexahydroxyl-tribenzocyclyne, topologically resembling the archetypal 3-fold symmetry 2,3,6,7,10,11-hexahydroxytriphenylene ligand. The design and choice of the alkyne moiety containing ligand (and thus of the resulting MOF) was multifold: conjugation within the ligand to maintain charge delocalization, increased ligand dimensions to augment pore size, and highly important, in the context of this work, installation of alkyne groups to permit postsynthetic metalation through alkyne-π coordination of d metals. The authors thus exploited established alkyne chemistry to host and absorb heterometal ions (e.g., Ni^{2+} and Co^{2+}) resulting in electrical conductivity changes due to intervalence charge transfer between the inserted metal and the MOF. A complementary strategy that nevertheless relied on a presynthetic methodology was also recently suggested by Lu et al.,[22] wherein hexaiminotriazatruxene ligands were first alkylated with alkyl chains of varying lengths, resulting in decreased electronic interaction as the interlayer distance within the generated MOFs increased.

Herein, we present two new 2D-e-MOFs based on nitrogen-rich 2,3,8,9,14,15-hexaaminotribenzimidazole (HATBim) and chemically reactive 2,3,7,8,12,13-hexaaminotriazatruxene (HATAT) ligands. The new MOFs, $Ni_3(HITAT)_2$ and $Ni_3(HITBim)_2$, reveal bulk temperature-activated charge transport, with electrical conductivity values of 44 and 0.5

$mS\ cm^{-1}$, respectively. $Ni_3(HITBim)_2$ reveals a large surface area of up to 1169 $m^2\ g^{-1}$, comparable to previously reported and topologically related $Cu_3(HHTT)_2$[23] and Cu-HHTC,[21] among the highest in this class.[1] The incorporation of triazatruxene core into the $Ni_3(HITAT)_2$ MOF structure preserves the chemical characteristics of the indole moiety, allowing for postsynthetic functionalization. We selected the mesylation reaction of indole N−H reactive site for the proof-of-concept demonstration of postsynthetic MOF pore functionalization and found that mesylation serves as a method to smoothly modulate electrical conductivity by a factor of nearly 20.

■ RESULTS AND DISCUSSION

The rationale behind the design of the two linkers used here is multifold and relates to the similar topology (for direct comparison) yet different electronic structure and chemical reactivity. First, the presence of nitrogen heteroatoms in the organic core is expected to reduce its electron density, resulting in a lower energy level for the lowest unoccupied molecular orbital (LUMO), strengthening the p-type character of the material (for example, as compared to prototypical HHTP-2,3,6,7,10,11-hexahydroxytriphenylene). Enlarging the π-conjugation facilitates stronger noncovalent interactions between adjacent molecules, promoting enhanced electrical conductivity in the resulting MOFs. For example, Dou et al. reported that by embedding nitrogen atoms into the ligand backbone (2,3,7,8,12,13-hexahydroxy tetraazanaphthotetraphene,
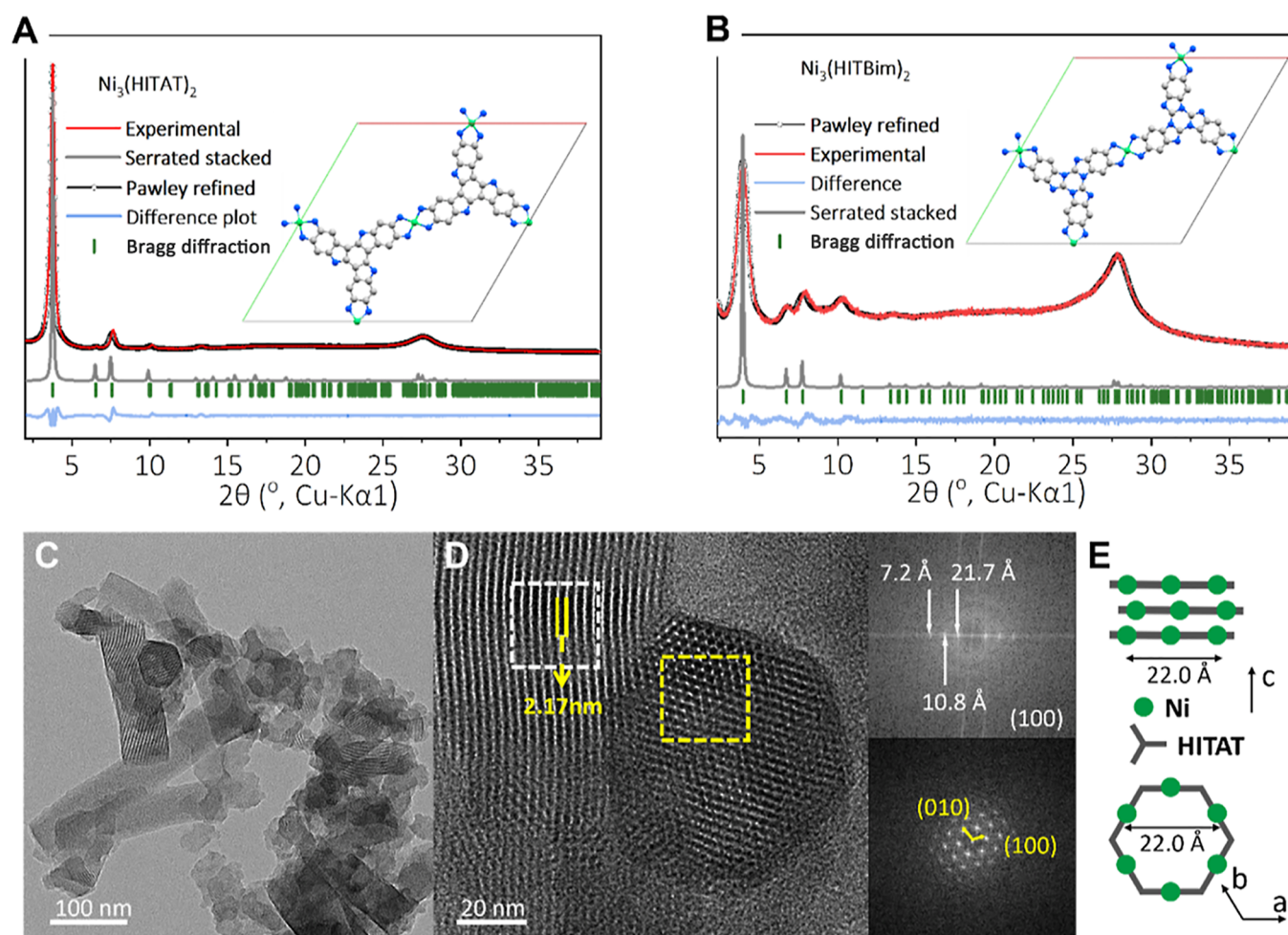
Figure 2. Structural characterization of $Ni_3(HITBim)_2$ and $Ni_3(HITAT)_2$. (A,B) Pawley refinement of PXRD data with experimental (red), simulated (gray), and difference (blue) patterns for $Ni_3(HITBim)_2$ and $Ni_3(HITAT)_2$. Low- (C) and high-(D) magnification HRTEM images of $Ni_3(HITAT)_2$ with fast Fourier transform analysis of the corresponding areas indicated by white (imaged normal to the c direction) and yellow squares (imaged along the c direction) (D, inset). (E) Schematic structure of $Ni_3(HITAT)_2$ to illustrate the (100) and (010) imaging orientations.

HHTT), stronger noncovalent interactions between conjugated molecules and balanced in-plane interactions were achieved, resulting in anisotropic growth with crystals reaching up to 200 μm in size. With these precise structural details, it was thus possible to demonstrate anisotropic in-plane and out-of-plane transport, establishing structure−conductivity relationships.[23]

Both HATAT and HATBim ligands exhibit contrasting chemical structures and have a larger π-conjugated core than the triphenylene core in 2,3,6,7,10,11-hexaaminotriphenylene (HATP) in stereotypical $Ni_3(HITP)_2$. The size of the conjugated core is known to significantly impact both the intra- and interligand interactions and to influence the crystallization and growth of the respective MOF.[23] The tribenzimidazole core in HATBim is an 18π-electron heteroaromatic system, with six electrons supplied by the nitrogen atoms. The electrostatic potential of HATAT displays a uniformly delocalized orbital over the entire ligand moiety, whereas the presence of the three supplementary embedded N atoms in HATBim translates into an electron-deficient ligand core and a lower LUMO (higher electro-affinity) relative to HATAT (Figure 1).

Finally, the main advantage of HATAT over HATP, HATBim, and other planar conjugated ligands is the presence of the indole functionality, a five-membered nitrogen-containing ring with a large aromatic system that displays extended electron delocalization (see Figures 1 and S1 for details), with reactive sites for potential derivatization (e.g., N-alkylation) at the N_5-, N_{10}-, and N_{15}- atoms (Figure 1).[24] Functionalization of the ligands provides the potential to tune the conductivity of the e-MOFs by increasing the degree of aggregation through peripheral derivatization or by grafting electron donor or acceptor groups.[22,25] The selection of HATAT and HATBim as the coordinating ligands was thus motivated not only by the concept of embedded heteroatoms but also by the possibility of postsynthetic functionalization at the N−H reactive sites of the triazatruxene moiety.

Synthesis and Structural Characterization of HATAT, HATBim, and the Respective MOFs—$Ni_3(HITAT)_2$ and $Ni_3(HITBim)_2$. Different synthetic routes were explored for the synthesis of the targeted hexaaminotriazatruxene (HATAT) and hexaaminotribenzimidazole (HATBim) linkers. The oxidative cyclotrimerization of indole, when carried out in the presence of excess bromine,[26] resulted in the formation of 2,3,7,8,12,13-hexabromotriazatruxene. Conversely, in the case of HATBim, the process involves the trimerization of 5,6-dibromo-2-chloro-1H-benzimidazole. Buchwald−Hartwig amination[27] was used for both ligands, entailing the peripheral
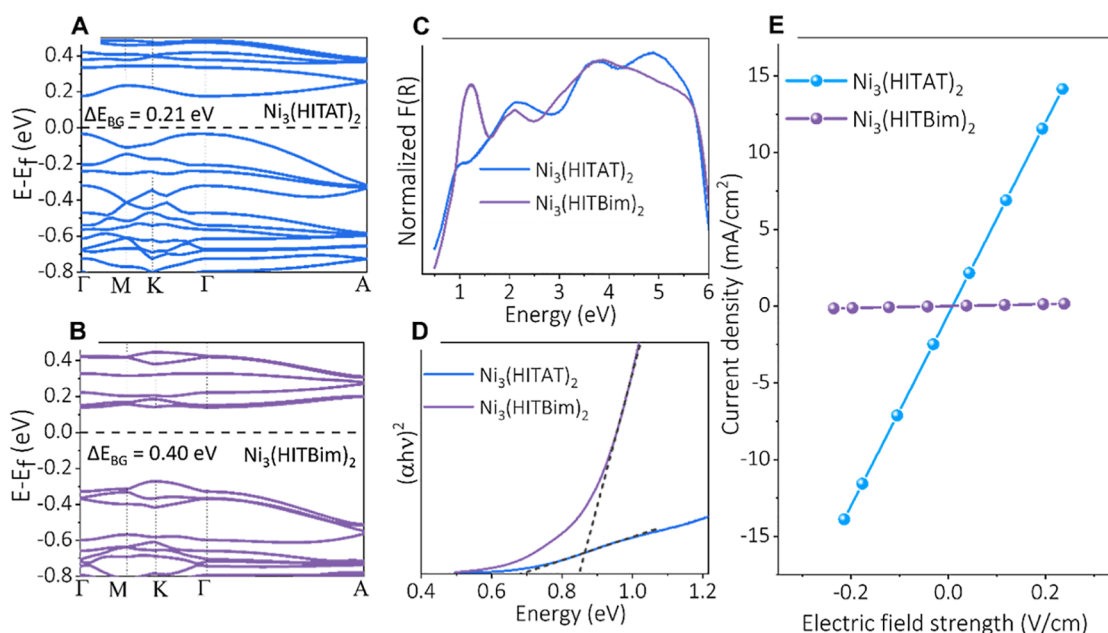
Figure 3. Charge transport properties of the $Ni_3(HITAT)_2$ and $Ni_3(HITBim)_2$ MOFs. Computed band structures of bulk $Ni_3(HITAT)_2$ (A) and $Ni_3(HITBim)_2$ (B). Normalized Kubelka–Munk-transformed spectra of $Ni_3(HITAT)_2$ and $Ni_3(HITBim)_2$ (C). The corresponding Tauc plots are calculated from the diffuse reflectance spectra (D). The extrapolated dashed lines represent linear fits to the absorption edges. Room-temperature current density vs electric field plots for $Ni_3(HITAT)_2$ and $Ni_3(HITBim)_2$ as measured on pressed powder form samples in a two-point probe configuration (E).

hexabromo-substituted intermediates (refer to the Supporting Information for experimental and synthesis details and Schemes S1 and S2). The synthesis conditions for $Ni_3(HITAT)_2$ and $Ni_3(HITBim)_2$ MOFs were next optimized by departing from the analogous approaches used for the synthesis of $Ni_3(HITP)_2,^{28}$ including adjusting the concentration of base, choice of solvents, and varying reaction temperatures (Figure S2). The optimal conditions for $Ni_3(HITAT)_2$ and $Ni_3(HITBim)_2$ MOFs' synthesis can be resumed to reacting a basic solution of $Ni(OAc)_2$ $4H_2O$ in a dimethylformamide (DMF)/dimethylacetamide (DMA) mixture with an aqueous solution of the respective ligands, followed by stirring under air at 65 °C, resulting in the formation of the target MOF (see the Supporting Information for experimental details and Figure S3).

Scanning electron microscopy (SEM) analysis of the prepared MOFs revealed that $Ni_3(HITAT)_2$ consists of hexagonal rods with variable length between 100 and 400 nm and smaller crystallites sizes of up to 50 nm length for $Ni_3(HITBim)_2$ (see Figure S4A,B). High-resolution X-ray photoelectron spectroscopy (XPS) analysis of the Ni(2p) and N1(1s) regions revealed only one type of Ni atom ($2p_{3/2}$, 855.4 eV) and two types of N atoms for both MOFs. These are attributed to the benzenoid amine N, $-NH-$ (399.5 eV) and quinoid imine $C=N-M$ (397.4 eV) in the $Ni_3(HITAT)_2$ structure (Figure 1) and quinoid imine (398.1 eV) and graphitic N (400.9 eV) for $Ni_3(HITBim)_2$ (refer to Figure S5 for details). The XPS analysis did not reveal any residual signature of Cl(2p) or Na(1s), which combined with the absence of the characteristic stretching bands of the CH_3COO^- group in Fourier transform infrared (FTIR) spectra (Figure S6) confirmed the charge-neutral nature of $Ni_3(HITAT)_2$ and $Ni_3(HITBim)_2$, consistent with previous observations on related 2D-based MOFs such as $Ni_3(HITP)_2$ and $Cu_3(HITP)_2.^{6,29}$

Powder X-ray diffraction (PXRD) analysis of $Ni_3(HITAT)_2$ revealed a crystalline phase, evidenced by prominent peaks at 2θ (Cu $K\alpha1$) = 3.76, 6.53, 7.57, 9.90, 13.11, and 27.67°. These are in good agreement with long-range ab plane growth with a serrated layered arrangement (Figures 2A and S7). The PXRD of $Ni_3(HITBim)_2$ (Figure 2B) has a qualitatively comparable pattern to $Ni_3(HITAT)_2$ but displays less intense and broadened diffraction peaks indicative of lower crystallinity and smaller particle size, corroborated by SEM analysis (Figure S4B). The structural elucidation for both MOFs was determined through simulation and Pawley refinement of PXRD experimental data with the unit cell parameters listed in Table S1. Considering the geometry of the ligands, four conformations (i.e. inclined, eclipsed, serrated, and staggered, refer to Figure S7 for details) were considered. Plane-wave van der Waals-corrected density functional theory (DFT) calculations revealed that the $Ni_3(HITAT)_2$ is not stable in the cofacial (eclipsed) stacking mode. The most stable conformations of $Ni_3(HITAT)_2$ were found to correspond to the inclined and serrated stacking, with an interlayer shift of $0.1*a$ and $0.1*b$, as shown in Figure S8. A good match with the experimental PXRD pattern is, however, observed only for the serrated stacking mode (Figures 2A,B, and S7). The broad peaks centered around $2\theta = 27.82°$ [$Ni_3(HITBim)_2$) and $2\theta = 27.67°$ ($Ni_3(HITAT)_2$] correspond to the (001) plane, revealing comparable interlayer spacings in the MOFs ($Ni_3(HITBim)_2$—3.18 Å and $Ni_3(HITAT)_2$—3.19 Å), which are in good agreement with the reported isostructural 2D-e-MOFs.^{6,17}

High-resolution transmission electron microscopy (HRTEM) of $Ni_3(HITAT)_2$ revealed long-range ordering along the three crystallographic directions (Figure 2C) and confirmed the expected honeycomb framework (Figure 2D, yellow square) defining parallel channels with the spacing between wavy fringes of 2.17 nm [Figure 2D, white square,

calculated from the fast Fourier transform (FFT) analysis]. These corroborate with the size defined by the distance of the nickel atoms at the opposite sides of the hexagon obtained from the PXRD analysis of $Ni_3(HITAT)_2$ (Φ = 22 Å, Figure 2E, bottom). FFT analysis of the HRTEM data also confirmed the atomically flat sheet orientation and evidence of stacking in the reciprocal lattice. The honeycomb-like 2D layered stacking along the c-axis ensures a guest-accessible mesoporous nature with a Barrett−Joyner−Halenda (BJH) adsorption pore diameter (4 V/A) of 17.95 and 17.39 Å for $Ni_3(HITBim)_2$ and $Ni_3(HITAT)_2$, respectively. These values are comparable to the predicted 19.03 Å ($Ni_3(HITAT)_2$) and 19.11 Å ($Ni_3(HITBim)_2$) pore sizes from the model structure (defined by the distance of the hydrogen atoms at the opposite sides of the hexagon). The N_2 adsorption isotherm revealed a Brunauer−Emmett−Teller (BET) surface area of 1169 and 679 m^2 g^{-1} (Figure S9), with a corresponding BJH adsorption cumulative pore volume of 0.55 and 0.43 cm^3 g^{-1} for $Ni_3(HITBim)_2$ and $Ni_3(HITAT)_2$, respectively. The large BET surface area for $Ni_3(HITBim)_2$, being among the highest values for nickel-based 2D-e-MOFs and comparable to $Cu_3(HHTT)_2$[23] and Cu-HHTC[21] 2D-MOF analogues, surpasses the values of previously reported 2D-e-MOFs (typically in the range of 300−600 m^2 g^{-1}) (Table S2).[21]

Charge Transport Analysis in $Ni_3(HITAT)_2$ and $Ni_3(HITBim)_2$. The topological and compositional differences between the ligands naturally lead to different degrees of electron delocalization, interlayer spacing, and $\pi-\pi$ inter-actions, which are most naturally reflected in the optoelectronic properties of $Ni_3(HITAT)_2$ and $Ni_3(HITBim)_2$ (Figure 3). Computed electronic band structures of bulk $Ni_3(HITAT)_2$ and $Ni_3(HITBim)_2$ suggest that the two MOFs are narrow-bandgap semiconductors (0.21, and 0.40 eV, Figure 3A,B, respectively). While $Ni_3(HITAT)_2$ shows significant electronic band dispersion along both the intraplane (K−Γ−M) and the interplane (A−Γ) vector directions (Figure 3A), the intraplane electronic band dispersion of $Ni_3(HITBim)_2$ is significantly suppressed and contrasts with the interplane direction, where band dispersion is augmented (Figure 3B, refer also to Figure S10 for additional details). The computed bulk hole (electron) effective mass values for $Ni_3(HITAT)_2$ are $m_h \approx 0.35\ m_0$ ($m_e \approx 0.41m_0$) and $m_h \approx 0.12\ m_0$ ($m_e \approx 1.37m_0$) along the intra- and interplane directions, respectively, as compared to $m_h \approx 0.67\ m_0$ ($m_e \approx 3.18m_0$) and $m_h \approx 0.51\ m_0$ ($m_e \approx 1.93m_0$) found in $Ni_3(HITBim)_2$ along the intra- and interplane directions, respectively. These differences imply that the chemical modification of HITBim vs HITAT ligands alters both the in-plane and out-of-plane charge transport (Figures S10 and S11). This result highlights that the nitrogen-rich core of the HITBim ligand does not contribute significantly to bands around the Fermi level, leading to minimal in-plane electronic dispersion between the ligands. This confirms the expectations based on molecular calculations, wherein a larger π-system containing more heteroatoms should stabilize electrons, resulting in diminished band dispersion (or delocalization).[30]

While it is hard to ascertain the sign of the majority charge carriers from our available experiments, a comparative assessment with the theoretical effective mass values, used here as a proxy for electrical conductivity, clearly indicates that $Ni_3(HITAT)_2$ should exhibit superior transport properties relative to $Ni_3(HITBim)_2$ irrespective of the type of majority charge carrier. The optical band gaps measured by UV−vis−NIR spectroscopy (Figure 3C) and extracted through linear fits

of the onset of the Tauc plot (Figures 3D and S12) were found to be 0.68 and 0.85 eV for $Ni_3(HITAT)_2$ and $Ni_3(HITBim)_2$, respectively. The electronic bandgaps of $Ni_3(HITAT)_2$ and $Ni_3(HITBim)_2$ monolayer forms are found to be 0.532 (0.74) eV and 0.535 (0.73) eV (Figure S10), respectively, at the GGA/PBE (HSE06) level of theory, while in the bulk forms, the electronic bandgaps are 0.21 and 0.40 eV, respectively (Figure 3A,B); the discrepancy between the estimated optical and calculated band gaps is explained by the limitation of the spectrometer at ~0.5 eV, which precludes observation of other potential absorption bands at lower energy. Although the experimental and computed values of the bandgaps are quantitatively different, they follow the same trend with a larger bandgap for $Ni_3(HITBim)_2$ relative to $Ni_3(HITAT)_2$. The room-temperature electrical conductivities of $Ni_3(HITAT)_2$ and $Ni_3(HITBim)_2$ MOFs, measured on pressed powders (refer to the Supporting Information for experimental details), were found to be 44 and 0.5 mS cm^{-1}, respectively (Figure 3E), whereas the activation energy for charge transport was extracted from the Arrhenius plot of 66 meV for $Ni_3(HITAT)_2$ and 220 meV for $Ni_3(HITBim)_2$ (Figure S13). Considering the difference in length of rod-like-shaped crystallites of the MOFs (Figure S4A,B), it is worth assuming that the measured values are underestimated due to the potentially anisotropic nature of charge transport, as well as additional contact and grain boundary resistances. Although the contributions are difficult to quantify, these are assumed to be reasonably similar for the $Ni_3(HITAT)_2$ and $Ni_3(HITBim)_2$ samples and the conductivity values mainly influenced by distinct aromatic cores within the MOF. It is noteworthy that the measured electronic conductivities are within range of the most highly conducting porous MOFs reported[1] (Table S2). For instance, the conductivity value of $Ni_3(HITAT)_2$ is nearly ten times higher than that of topologically similar truxene-Cu MOF[31] and truxone−Cu MOF[32] and approximately 90 times higher than that of $Ni_3(HITBim)_2$ (Table S2).

Terahertz spectroscopy experiments were recently employed to show that while the intraplane charge transport follows a band-like behavior, thermally activated interplane hopping appears to be the bottleneck for charge transport in 2D-e-MOF materials.[33−36] From the combined experimental and theoretical analysis, $Ni_3(HITAT)_2$ is found to exhibit not only lower hole/electron effective masses but also lower activation energy of ≈66 meV, as compared to ≈220 meV for $Ni_3(HITBim)_2$ (Figure S13). HATAT is thus found to enhance the charge transport properties in $Ni_3(HITAT)_2$, likely owing to both modulation of the energy of the Frontier orbitals and enhancement of the crystalline packing between layers, corroborating earlier findings.[23] Considering the nearly similar interlayer spacing of $Ni_3(HITAT)_2$ (3.19 Å), its enhanced conductivity could be attributed to improved in-plane electron delocalization, whereas in the case of $Ni_3(HITBim)_2$, with an interlayer spacing of 3.18 Å, the higher effective hole and electron mass results in lower conductivity values. It is therefore probable that in $Ni_3(HITBim)_2$, interlayer charge hopping is dominant owing to the ineffective in-plane orbital mixing. This observation corroborates previous findings for rare-earth-based HOTP materials.[37]

Postsynthetic Functionalization and Charge Transport Modification in $Ni_3(HITAT)_2$. To explore the specific role of the HITAT ligand and the functionalization of the indole unit within the triazatruxene moiety of $Ni_3(HITAT)_2$, we employed N-functionalization as proof of concept for the
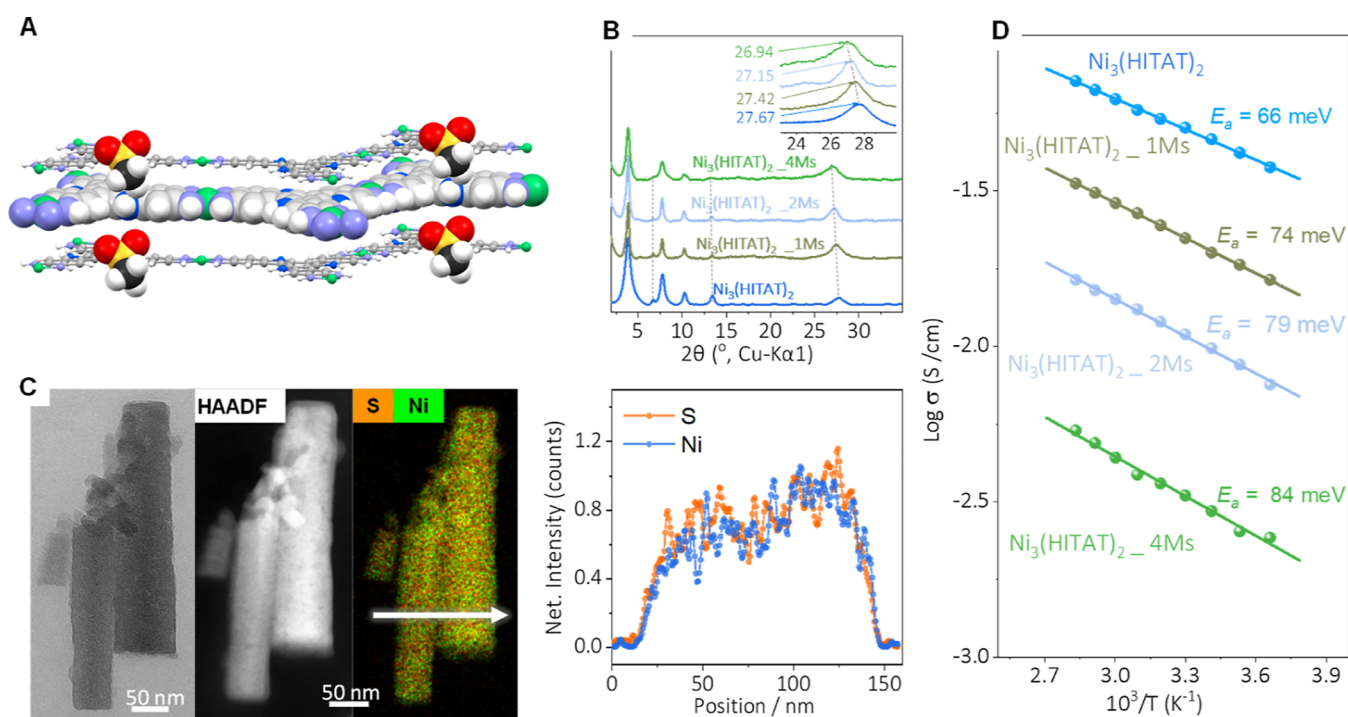
Figure 4. (A) Schematic illustration of functionalized $Ni_3(HITAT)_2$ layers highlighting the sterically bulky mesyl-grafted layers. Atomic distances to scale. Legend: red balls: O; gray/black balls: C; white balls: H; blue balls: N; green balls: Ni. (B) PXRD data of pristine $Ni_3(HITAT)_2$ and functionalized $Ni_3(HITAT)_2$_xMs (x: 1, 2, 4) samples. Inset: zoom on the 001-diffraction region highlighting proportionality to the mesylation extent shift of the 001 peak. (C) TEM images of $Ni_3(HITAT)_2$_2Ms (left), the corresponding high-angle annular dark-field scanning transmission electron microscope image (middle) and associated EDX map and EDX-line scanning profile of Ni and S elements (right). (D) Arrhenius plot of electrical conductivity and estimated activation energy of transport for the $Ni_3(HITAT)_2$_xMs series.

postsynthetic modification of 2D-e-MOFs (Figure 4A). Importantly, the ligand unit in $Ni_3(HITAT)_2$ maintained its aromaticity despite being oxidized, with the indole N−H prone to chemical modification.[30] We selected functionalization of triazatruxene via mesylation: the $CH_3−SO_2^-$ group provides a convenient FTIR handle with its specific stretch band at 1050−1250 cm^{-1}, while sulfur can be easily detected and quantified by microelemental analysis. Mesylation was attempted by reacting pristine $Ni_3(HITAT)_2$ with varying equivalents of methanesulfonyl chloride ($CH_3−SO_2−Cl$, MsCl). Specifically, $Ni_3(HITAT)_2$ was first activated at 100 °C (Figure S14), dispersed in dry tetrahydrofuran, and the suspension was treated with NaH followed by the addition of methanesulfonyl chloride (refer to the Supporting Information for experimental details). Elemental analysis confirmed the progressive mesylation with approximately 1, 2, and 4 [$CH_3−SO_2^-$] groups per formula unit of $Ni_3(HITAT)_2$, these being noted hereafter as $Ni_3(HITAT)_2$_xMs (x = 1, 2, and 4). Complete mesylation (i.e., formation of $Ni_3(HITAT)_2$_6Ms), was not attained, most certainly prevented by the large steric repulsion of the mesyl groups.

Structurally, grafting the mesyl groups should primarily perturb the interlayer spacing due to the van der Waals repulsion between the meslyl groups on adjacent layers. Experimentally, there were indeed no noticeable changes in the low-angle PXRD peaks, yet a measurable shift of the 001 reflection peak from 27.67° in $Ni_3(HITAT)_2$ to 27.42, 27.15, and 26.94° in $Ni_3(HITAT)_2$_1Ms, $Ni_3(HITAT)_2$_2Ms, and $Ni_3(HITAT)_2$_4Ms, respectively, was noted (Figure 4B). According to the Bragg equation, the interlayer distance increased from 3.19 Å [in pristine $Ni_3(HITAT)_2$] to 3.30 Å

[for $Ni_3(HITAT)_2$_4Ms]. Based on the SEM images, the hexagonal rods of pristine $Ni_3(HITAT)_2$ MOF, which originally measured 100−400 nm in size, have been reduced in size in the mesylated MOF samples (below 100 nm) (Figure S15). Additionally, a decrease in the intensity of peaks at 6.69 and 13.37° (Figure 4B, highlighted with dashed lines) is noted with these corresponding to d_{120} = 13.68 Å and d_{240} = 6.84 Å, matching well with the simulated 2D $Ni_3(HITAT)_2$ structure (Figure S16). The decrease in the intensity of the respective peaks indicates that the scattering of X-rays from crystallographic planes has weakened as a result of distortions in the crystal lattice, induced by mesyl grafting onto the indole N−H moiety.

To further confirm the chemical functionalization and robustness of $Ni_3(HITAT)_2$, additional physicochemical characterization was performed. TEM and SEM images of the functionalized $Ni_3(HITAT)_2$_2Ms show that the nanorod morphology is preserved (Figures 4C and S15), proving the structural stability upon applied postsynthetic functionalization. Energy-dispersive X-ray (EDX) elemental mapping (image and line profile, Figure 4C) shows uniform distribution of sulfur within the MOF rods, confirming homogeneous grafting within the $Ni_3(HITAT)_2$ pores and not only at the surface. FTIR analysis of all functionalized $Ni_3(HITAT)_2$_xMs (x = 1, 2, 4) revealed a band at ∼1189 and 1065 cm^{-1}, characteristic of the $−SO_2^-$ stretch, with the signal intensity increasing proportionally with the equivalent of Ms grafted (Figure S6C). Broadening of the aromatic ring vibration (1429 cm^{-1}) and the increased intensity of the $C_2 > N−$ band (≈1298 cm^{-1}) upon mesylation (Figure S6C) provide additional confirmation of postsynthetic chemical modification

of $Ni_3(HITAT)_2$. Finally, note that the mesylation resulted in a proportional decrease of BET surface area to 567.3 m^2 g^{-1} in $Ni_3(HITAT)_2\_1Ms$, 525.6 m^2 g^{-1} in $Ni_3(HITAT)_2\_2Ms$, and 387.4 m^2 g^{-1} in $Ni_3(HITAT)_2\_4Ms$, with a corresponding reduction in the BJH adsorption cumulative pore volume to 0.42, 0.38, and 0.25 cm^3 g^{-1}, respectively (Figure S17).

Notably, increasing the degree of mesylation resulted in a proportional decrease in the electrical conductivity at room temperature, with $Ni_3(HITAT)_2\_1Ms$, $Ni_3(HITAT)_2\_2Ms$, and $Ni_3(HITAT)_2\_4Ms$ exhibiting values of 21.2, 9.6, and 2.7 mS cm^{-1}, respectively (Figure S18), displaying a variation by a factor of nearly 20 as compared to pristine $Ni_3(HITAT)_2$ (i.e., conductivity of 44 mS cm^{-1}). Variable temperature transport measurements revealed temperature-activated, semiconducting-like transport behavior for all compositions. The activation energies for transport were found to correlate well with the σ values: 74 meV for $Ni_3(HITAT)_2\_1Ms$, 79 meV for $Ni_3(HITAT)_2\_2Ms$, and 84 meV for $Ni_3(HITAT)_2\_4Ms$ (Figure 4D)—displaying a monotonic increase with Ms group content—providing an additional confirmation of continuous compositional band engineering through post-synthetic functionalization.

In the $Ni_3(HITAT)_2\_xMs$ (x: 1, 2, 4) series, the decrease in conductivity is attributed to a combination of concurrent factors. The shift toward lower angles of the (001) reflection, corresponding to the $\pi-\pi$ stacking, indicates a more distanced interlayered structure, which would inhibit interlayer hopping of charge carriers and reduce the overlap integral between the orbitals of p parentage on adjacent layers. This corroborates with previous reports on hexaiminotriazatruxene-based MOFs, with ligands modified by alkyl chains with different lengths, showing a similar trend of decreased electronic interaction with increasing interlayer distance.[22] DFT calculations further support that grafting mesyl groups leads to an increase in both intra- and interlayer effective masses for holes and electrons (Figure S19). This is due to the intraplane structural disorder, the increased interlayer spacing, and the electron-withdrawing character of the grafted mesyl groups, which result in a flattening of the bands in the mesylated $Ni_3(HITAT)_2$ materials, ultimately leading to lower conductivity values, as confirmed experimentally.

◼ CONCLUSIONS

In this work, we show how embedding nitrogen heteroatoms within two isostructural C_3-symmetric ligands, HITAT and HITBim, alters both in-plane and out-of-plane charge transport characteristics of the resulting MOFs. It is found that interlayer charge transport is dominant owing to ineffective in-plane orbital mixing in $Ni_3(HITBim)_2$, as opposed to that in the $Ni_3(HITAT)_2$ composition. Grafting electron-withdrawing mesyl groups on $Ni_3(HITAT)_2$ increases the interlayer spacing and depletes the electron density within the core of HITAT, affecting the charge carrier mobility and concentration, which further leads to the decrease of the conductivity of the material. Overall, this work offers a novel view to develop electrically tunable conductive 2D-MOFs via postsynthetic functionalization that, with feasible functional groups, can provide alternative information on the structure−conductivity relationship.

◼ ASSOCIATED CONTENT

Data Availability Statement

The data sets generated and analyzed in this study are included in the paper and its Supporting Information or available from the corresponding author upon reasonable request.

ⓢ Supporting Information

The Supporting Information is available free of charge at https://pubs.acs.org/doi/10.1021/jacs.3c07503.

Materials and methods, experimental procedures for synthesis and characterization data of ligands and MOFs, and computation details (PDF)

◼ AUTHOR INFORMATION

Corresponding Authors

Petru Apostol — *Institute of Condensed Matter and Nanosciences, Molecular Chemistry, Materials and Catalysis, Université Catholique de Louvain, Louvain-la-Neuve B-1348, Belgium;* Email: petru.apostol@uclouvain.be

Alexandru Vlad — *Institute of Condensed Matter and Nanosciences, Molecular Chemistry, Materials and Catalysis, Université Catholique de Louvain, Louvain-la-Neuve B-1348, Belgium;* ⓞ orcid.org/0000-0002-0059-9119; Email: alexandru.vlad@uclouvain.be

Authors

Sai Manoj Gali — *Laboratory for Chemistry of Novel Materials, Materials Research Institute, Université de Mons, Mons 7000, Belgium;* ⓞ orcid.org/0000-0002-0388-7888

Alice Su — *Department of Chemistry, Massachusetts Institute of Technology, Cambridge, Massachusetts 02139-4307, United States*

Da Tie — *Institute of Condensed Matter and Nanosciences, Molecular Chemistry, Materials and Catalysis, Université Catholique de Louvain, Louvain-la-Neuve B-1348, Belgium*

Yan Zhang — *Institute of Condensed Matter and Nanosciences, Molecular Chemistry, Materials and Catalysis, Université Catholique de Louvain, Louvain-la-Neuve B-1348, Belgium*

Shubhadeep Pal — *Institute of Condensed Matter and Nanosciences, Molecular Chemistry, Materials and Catalysis, Université Catholique de Louvain, Louvain-la-Neuve B-1348, Belgium*

Xiaodong Lin — *Institute of Condensed Matter and Nanosciences, Molecular Chemistry, Materials and Catalysis, Université Catholique de Louvain, Louvain-la-Neuve B-1348, Belgium;* ⓞ orcid.org/0000-0002-1867-4789

Vasudeva Rao Bakuru — *Institute of Condensed Matter and Nanosciences, Molecular Chemistry, Materials and Catalysis, Université Catholique de Louvain, Louvain-la-Neuve B-1348, Belgium*

Darsi Rambabu — *Institute of Condensed Matter and Nanosciences, Molecular Chemistry, Materials and Catalysis, Université Catholique de Louvain, Louvain-la-Neuve B-1348, Belgium*

David Beljonne — *Laboratory for Chemistry of Novel Materials, Materials Research Institute, Université de Mons, Mons 7000, Belgium;* ⓞ orcid.org/0000-0002-2989-3557

Mircea Dincă — *Department of Chemistry, Massachusetts Institute of Technology, Cambridge, Massachusetts 02139-4307, United States;* ⓞ orcid.org/0000-0002-1262-1264

Complete contact information is available at:
https://pubs.acs.org/10.1021/jacs.3c07503

■ REFERENCES

(1) Xie, L. S.; Skorupskii, G.; Dincă, M. Electrically Conductive Metal-Organic Frameworks. *Chem. Rev.* **2020**, *120* (16), 8536−8580.

(2) Qiu, T.; Liang, Z.; Guo, W.; Tabassum, H.; Gao, S.; Zou, R. Metal-Organic Framework-Based Materials for Energy Conversion and Storage. *ACS Energy Lett.* **2020**, *5* (2), 520−532.

(3) Rambabu, D.; Lakraychi, A. E.; Wang, J.; Sieuw, L.; Gupta, D.; Apostol, P.; Chanteux, G.; Goossens, T.; Robeyns, K.; Vlad, A. An Electrically Conducting Li-Ion Metal-Organic Framework. *J. Am. Chem. Soc.* **2021**, *143* (30), 11641−11650.

(4) Morozan, A.; Jaouen, F. Metal Organic Frameworks for Electrochemical Applications. *Energy Environ. Sci.* **2012**, *5* (11), 9269−9290.

(5) Kreno, L. E.; Leong, K.; Farha, O. K.; Allendorf, M.; Van Duyne, R. P.; Hupp, J. T. Metal-Organic Framework Materials as Chemical Sensors. *Chem. Rev.* **2012**, *112* (2), 1105−1125.

(6) Sheberla, D.; Sun, L.; Blood-Forsythe, M. A.; Er, S.; Wade, C. R.; Brozek, C. K.; Aspuru-Guzik, A.; Dincă, M. High Electrical Conductivity in Ni $_3$ (2,3,6,7,10,11-Hexaiminotriphenylene) $_2$, a Semiconducting Metal-Organic Graphene Analogue. *J. Am. Chem. Soc.* **2014**, *136* (25), 8859−8862.

(7) Kobayashi, Y.; Jacobs, B.; Allendorf, M. D.; Long, J. R. Conductivity, Doping, and Redox Chemistry of a Microporous Dithiolene-Based Metal-Organic Framework. *Chem. Mater.* **2010**, *22* (14), 4120−4122.

(8) Day, R. W.; Bediako, D. K.; Rezaee, M.; Parent, L. R.; Skorupskii, G.; Arguilla, M. Q.; Hendon, C. H.; Stassen, I.; Gianneschi, N. C.; Kim, P.; Dincă, M. Single Crystals of Electrically Conductive Two-Dimensional Metal-Organic Frameworks: Structural and Electrical Transport Properties. *ACS Cent. Sci.* **2019**, *5* (12), 1959−1964.

(9) Liao, P.-Q.; Shen, J.-Q.; Zhang, J.-P. Metal-Organic Frameworks for Electrocatalysis. *Coord. Chem. Rev.* **2018**, *373*, 22−48.

(10) Wang, M.; Dong, R.; Feng, X. Two-Dimensional Conjugated Metal-Organic Frameworks (2D c-MOFs): Chemistry and Function for MOFtronics. *Chem. Soc. Rev.* **2021**, *50* (4), 2764−2793.

(11) Park, J.; Lee, M.; Feng, D.; Huang, Z.; Hinckley, A. C.; Yakovenko, A.; Zou, X.; Cui, Y.; Bao, Z. Stabilization of Hexaaminobenzene in a 2D Conductive Metal-Organic Framework for High Power Sodium Storage. *J. Am. Chem. Soc.* **2018**, *140* (32), 10315−10323.

(12) Li, P.; Wang, B. Recent Development and Application of Conductive MOFs. *Isr. J. Chem.* **2018**, *58* (9−10), 1010−1018.

(13) Kang, M.; Kang, D. W.; Hong, C. S. Post-Synthetic Diamine-Functionalization of MOF-74 Type Frameworks for Effective Carbon Dioxide Separation. *Dalton Trans.* **2019**, *48* (7), 2263−2270.

(14) Lyu, H.; Chen, O. I.-F.; Hanikel, N.; Hossain, M. I.; Flaig, R. W.; Pei, X.; Amin, A.; Doherty, M. D.; Impastato, R. K.; Glover, T. G.; Moore, D. R.; Yaghi, O. M. Carbon Dioxide Capture Chemistry of Amino Acid Functionalized Metal-Organic Frameworks in Humid Flue Gas. *J. Am. Chem. Soc.* **2022**, *144* (5), 2387−2396.

(15) Babaee, S.; Zarei, M.; Sepehrmansourie, H.; Zolfigol, M. A.; Rostamnia, S. Synthesis of Metal-Organic Frameworks MIL-101(Cr)-NH2 Containing Phosphorous acid Functional Groups: Application for the Synthesis of N-Amino-2-Pyridone and Pyrano [2,3-c]Pyrazole Derivatives via a Cooperative Vinylogous Anomeric-Based Oxidation. *ACS Omega* **2020**, *5* (12), 6240−6249.

(16) Kambe, T.; Sakamoto, R.; Hoshiko, K.; Takada, K.; Miyachi, M.; Ryu, J.-H.; Sasaki, S.; Kim, J.; Nakazato, K.; Takata, M.; Nishihara, H. π-Conjugated Nickel Bis(Dithiolene) Complex Nanosheet. *J. Am. Chem. Soc.* **2013**, *135* (7), 2462−2465.

(17) Hmadeh, M.; Lu, Z.; Liu, Z.; Gándara, F.; Furukawa, H.; Wan, S.; Augustyn, V.; Chang, R.; Liao, L.; Zhou, F.; Perre, E.; Ozolins, V.; Suenaga, K.; Duan, X.; Dunn, B.; Yamamto, Y.; Terasaki, O.; Yaghi, O. M. New Porous Crystals of Extended Metal-Catecholates. *Chem. Mater.* **2012**, *24* (18), 3511−3513.

(18) Clough, A. J.; Skelton, J. M.; Downes, C. A.; de la Rosa, A. A.; Yoo, J. W.; Walsh, A.; Melot, B. C.; Marinescu, S. C. Metallic Conductivity in a Two-Dimensional Cobalt Dithiolene Metal-Organic Framework. *J. Am. Chem. Soc.* **2017**, *139* (31), 10863−10867.

(19) Yang, C.; Dong, R.; Wang, M.; Petkov, P. S.; Zhang, Z.; Wang, M.; Han, P.; Ballabio, M.; Bräuninger, S. A.; Liao, Z.; Zhang, J.; Schwotzer, F.; Zschech, E.; Klauss, H.-H.; Cánovas, E.; Kaskel, S.; Bonn, M.; Zhou, S.; Heine, T.; Feng, X. A Semiconducting Layered Metal-Organic Framework Magnet. *Nat. Commun.* **2019**, *10* (1), 3260.

(20) Nagatomi, H.; Yanai, N.; Yamada, T.; Shiraishi, K.; Kimizuka, N. Synthesis and Electric Properties of a Two-Dimensional Metal-Organic Framework Based on Phthalocyanine. *Chem.—Eur. J.* **2018**, *24* (8), 1806−1810.

(21) Pham, H. T. B.; Choi, J. Y.; Huang, S.; Wang, X.; Claman, A.; Stodolka, M.; Yazdi, S.; Sharma, S.; Zhang, W.; Park, J. Imparting Functionality and Enhanced Surface Area to a 2D Electrically Conductive MOF via Macrocyclic Linker. *J. Am. Chem. Soc.* **2022**, *144* (23), 10615−10621.

(22) Lu, Y.; Zhang, Y.; Yang, C.-Y.; Revuelta, S.; Qi, H.; Huang, C.; Jin, W.; Li, Z.; Vega-Mayoral, V.; Liu, Y.; Huang, X.; Pohl, D.; Položij, M.; Zhou, S.; Cánovas, E.; Heine, T.; Fabiano, S.; Feng, X.; Dong, R. Precise Tuning of Interlayer Electronic Coupling in Layered Conductive Metal-Organic Frameworks. *Nat. Commun.* **2022**, *13* (1), 7240.

(23) Dou, J.-H.; Arguilla, M. Q.; Luo, Y.; Li, J.; Zhang, W.; Sun, L.; Mancuso, J. L.; Yang, L.; Chen, T.; Parent, L. R.; Skorupskii, G.; Libretto, N. J.; Sun, C.; Yang, M. C.; Dip, P. V.; Brignole, E. J.; Miller, J. T.; Kong, J.; Hendon, C. H.; Sun, J.; Dincă, M. Atomically Precise Single-Crystal Structures of Electrically Conducting 2D Metal-Organic Frameworks. *Nat. Mater.* **2021**, *20* (2), 222−228.

(24) Li, X.-C.; Wang, C.-Y.; Lai, W.-Y.; Huang, W. Triazatruxene-Based Materials for Organic Electronics and Optoelectronics. *J. Mater. Chem. C* **2016**, *4* (45), 10574−10587.

(25) Górski, K.; Mech-Piskorz, J.; Pietraszkiewicz, M. From Truxenes to Heterotruxenes: Playing with Heteroatoms and the Symmetry of Molecules. *New J. Chem.* **2022**, *46* (19), 8939−8966.

(26) Robertson, N.; Parsons, S.; MacLean, E. J.; Coxall, R. A.; Mount, A. R. Preparation, X-Ray Structure and Properties of a Hexabrominated, Symmetric Indole Trimer and Its TCNQ Adduct: A New Route to Functional Molecular Systems. *J. Mater. Chem.* **2000**, *10* (9), 2043−2047.

(27) Wolfe, J. P.; Wagaw, S.; Buchwald, S. L. An Improved Catalyst System for Aromatic Carbon-Nitrogen Bond Formation: The Possible Involvement of Bis(Phosphine) Palladium Complexes as Key Intermediates. *J. Am. Chem. Soc.* **1996**, *118* (30), 7215−7216.

(28) Chen, T.; Dou, J.-H.; Yang, L.; Sun, C.; Libretto, N. J.; Skorupskii, G.; Miller, J. T.; Dincǎ, M. Continuous Electrical Conductivity Variation in M3(Hexaiminotriphenylene)2 (M = Co, Ni, Cu) MOF Alloys. *J. Am. Chem. Soc.* **2020**, *142* (28), 12367−12373.

(29) Campbell, M. G.; Sheberla, D.; Liu, S. F.; Swager, T. M.; Dincǎ, M. Cu3(Hexaiminotriphenylene)2: An Electrically Conductive 2D Metal-Organic Framework for Chemiresistive Sensing. *Angew. Chem., Int. Ed.* **2015**, *54* (14), 4349−4352.

(30) Demuth, M. C.; Hendon, C. H. Linker Aromaticity Reduces Band Dispersion in 2D Conductive Metal-Organic Frameworks. *ACS Mater. Lett.* **2023**, *5* (5), 1476−1480.

(31) Zhao, Q.; Li, S.-H.; Chai, R.-L.; Ren, X.; Zhang, C. Two-Dimensional Conductive Metal-Organic Frameworks Based on Truxene. *ACS Appl. Mater. Interfaces* **2020**, *12* (6), 7504−7509.

(32) Zhao, Q.; Jiang, J.; Zhao, W.; Li, S.-H.; Mi, W.; Zhang, C. Truxone-Based Conductive Metal-Organic Frameworks for the Oxygen Reductive Reaction. *J. Phys. Chem. C* **2021**, *125* (23), 12690−12698.

(33) Zheng, W.; Sun, B.; Li, D.; Gali, S. M.; Zhang, H.; Fu, S.; Di Virgilio, L.; Li, Z.; Yang, S.; Zhou, S.; Beljonne, D.; Yu, M.; Feng, X.; Wang, H. I.; Bonn, M. Band Transport by Large Fröhlich Polarons in MXenes. *Nat. Phys.* **2022**, *18* (5), 544−550.

(34) Fu, S.; Jia, X.; Hassan, A. S.; Zhang, H.; Zheng, W.; Gao, L.; Di Virgilio, L.; Krasel, S.; Beljonne, D.; Tielrooij, K.-J.; Bonn, M.; Wang, H. I. Reversible Electrical Control of Interfacial Charge Flow across van Der Waals Interfaces. *Nano Lett.* **2023**, *23* (5), 1850−1857.

(35) Fu, S.; Jin, E.; Hanayama, H.; Zheng, W.; Zhang, H.; Di Virgilio, L.; Addicoat, M. A.; Mezger, M.; Narita, A.; Bonn, M.; Müllen, K.; Wang, H. I. Outstanding Charge Mobility by Band Transport in Two-Dimensional Semiconducting Covalent Organic Frameworks. *J. Am. Chem. Soc.* **2022**, *144* (16), 7489−7496.

(36) Ippolito, S.; Urban, F.; Zheng, W.; Mazzarisi, O.; Valentini, C.; Kelly, A. G.; Gali, S. M.; Bonn, M.; Beljonne, D.; Corberi, F.; Coleman, J. N.; Wang, H. I.; Samorì, P. Unveiling Charge-Transport Mechanisms in Electronic Devices Based on Defect-Engineered MoS2 Covalent Networks. *Adv. Mater.* **2023**, *35*, 2211157.

(37) Skorupskii, G.; Trump, B. A.; Kasel, T. W.; Brown, C. M.; Hendon, C. H.; Dincǎ, M. Efficient and Tunable One-Dimensional Charge Transport in Layered Lanthanide Metal-Organic Frameworks. *Nat. Chem.* **2020**, *12* (2), 131−136.